

Microstructure refinement for high modulus in-situ metal matrix composite steels via controlled solidification of the system Fe–TiB₂



H. Springer*, R. Aparicio Fernandez, M.J. Duarte, A. Kostka, D. Raabe

Max-Planck-Institut für Eisenforschung GmbH, 40237 Düsseldorf, Germany

ARTICLE INFO

Article history:

Received 17 December 2014

Revised 8 June 2015

Accepted 8 June 2015

Keywords:

Steel

Elastic modulus

Density

Metal-matrix-composites

Liquid metallurgy

ABSTRACT

Microstructures of Fe–TiB₂ metal-matrix-composites formed in-situ from Fe–Ti–B melts were investigated for hypo- and hyper-eutectic concentrations down to atomic-scale resolution. Special emphasis is laid on the influence of the solidification rate on particle size, morphology and distribution as well as their relation to mechanical properties. Innovative routes for the cost-effective production of stiff and ductile high modulus steels for lightweight structural applications are discussed, focusing on hyper-eutectic compositions due to their high stiffness/density ratio: firstly, very slow cooling allows the primary particles floating to the top of the cast, from which they can either be easily removed for retaining bulk material containing only fine-dispersed eutectic particles, or be kept and utilised as a wear resistant surface. Secondly, annealing of amorphous matrix material obtained from very fast solidification leads to fine dispersed nano-scaled precipitation of TiB₂ particles.

© 2015 Acta Materialia Inc. Published by Elsevier Ltd. All rights reserved.

1. Introduction

Structural material design aims at shifting technological frontiers by improving physical, chemical and mechanical properties. Among other driving forces such as improved corrosion resistance for longer component life [1–3], increased operating parameters for higher efficiency in energy conversion applications [4,5] and reduction of expensive alloying elements [6–8], weight reduction represents a major challenge for example to lower fuel consumption in transportation systems. Steels represent the most common class of high performance structural materials, as their multiple equilibrium and non-equilibrium phase transformations allow designing a wide spectrum of mechanical properties, and because iron (Fe) based alloys are easy to recycle and very cost-effective [9,10]. The comparatively high density (ρ) of Fe (7.86 g cm^{-3}) as the basic matrix element of steels, on the other hand, appears at first glance as a negative factor for weight reduction in structural engineering. However, the weight of a construction element is determined not only by the density of the chosen material, but also by the parts' volume, which in turn is resulting from the wall thickness required to avoid rupture and unduly elastic distortion under load. Ductility, i.e. the ability to undergo plastic deformation, is mainly required for forming operations in the parts' production, and adds safety in case of accidental overloading ('deformation before rupture') during its service life [11].

Therefore the key properties of structural materials for weight reduced parts maybe defined as (i) high yield strength in concert with a satisfactory amount of ductility, (ii) low ρ and (iii) a high Young's modulus (E) for high component stiffness. As it offers a similar specific modulus (E/ρ) as established light metals – such as aluminium, magnesium or titanium – of about $25 \text{ GPa cm}^3 \text{ g}^{-1}$ [11], Fe appears quite favourable in this context due to its aforementioned advantageous combination of intrinsic properties. The further reduction of ρ achievable by alloying additions of lighter elements, though, is typically accompanied by a decrease of E [12,13]. For example, in lightweight 'triplex' steels containing up to 11 wt.% Al, ρ could be reduced down to less than 7 g cm^{-3} , but E dropped simultaneously from $\sim 208 \text{ GPa}$ (pure Fe) to less than 170 GPa [14–16]. Depending on the application and its specific loading regime, compensation of this loss in inherent stiffness by a larger wall thickness can thus reduce or even eliminate the weight saving potential offered by such a lightweight alloy.

In order to overcome this detrimental relationship between E and ρ , the most promising material design strategy is to blend stiff and lightweight phases such as oxides, nitrides or carbides (as particles or fibres) with a ductile metal matrix, creating metal-matrix-composites (MMCs) [17–19]. Most of the previous works are concerned with Al-based MMCs fabricated by powder-metallurgical synthesis techniques, which offer very high flexibility and control in terms of particle type, size and dispersion [20–22]. The correspondingly increased efforts in material production, however, have so far limited the use of high stiffness/low density MMCs to niche applications [11,23]. These limiting factors may

* Corresponding author.

E-mail address: h.springer@mpie.de (H. Springer).

be overcome by the development of cost effective Fe-based MMCs, termed high modulus steels (HMS), most ideally synthesised by liquid metallurgy techniques [24–26]. Titanium-diboride (TiB_2) is a very attractive candidate material as particle-reinforcing compound for HMS, as it is very effective ($E \sim 565 \text{ GPa}$, $\rho \sim 4.25 \text{ g cm}^{-3}$ [27]) and can be created in-situ in the solid or liquid phase from an Fe–Ti–B precursor alloy [28,29]. Tanaka et al. [30] have thus fabricated a HMS – though via powder metallurgy synthesis – with a specific modulus of about $43 \text{ GPa cm}^3 \text{ g}^{-1}$ by incorporating about 30 vol.% TiB_2 in an Fe–Cr alloy.

However, the addition of such inherently brittle ceramic particles (K_{IC} of $\text{TiB}_2 \sim 4 - 7 \text{ MPa m}^{1/2}$ [27]) significantly deteriorates the materials' toughness and ductility [25,31–34]. This becomes especially relevant for the pseudo-binary system Fe– TiB_2 , where the large TiB_2 fractions (above $\sim 15 \text{ vol.}\%$) required for significant effects on E and ρ result in the formation of sharp-edged eutectic lamellae and coarse hyper-eutectic particles from the melt (eutectic concentration about 6.3 mol.% TiB_2 , [28,30]). In order to improve the mechanical properties – especially ductility – of HMS, it is thus of essential to achieve a more favourable, i.e. mechanically compliant, shape of the particles within the Fe matrix while using cost effective liquid metallurgy synthesis methods. A promising pathway lies in tailoring the primary precipitation and eutectic decomposition via the solidification rate, as it is well known for instance in tool steels, where networks of embrittling alloy-carbides can be significantly refined leading to increased toughness of the bulk material [9,34,35].

2. Objective

The objective of this work is to systematically study the effect of the solidification rate on morphology, size and dispersion of TiB_2 particles formed in-situ from Fe–Ti–B melts. The relationship between particle morphology and mechanical response as a function of the TiB_2 content is investigated as a key parameter to the knowledge based alloy design of HMS with an optimised profile of both physical and mechanical properties.

3. Materials and methods

Two alloy compositions were investigated in this work: (i) a hypo- and (ii) a hyper-eutectic alloy with the nominal compositions Fe – 4.61 Ti – 1.78 B and Fe – 10.10 Ti – 3.86 B, respectively (all in wt.%). The two alloy concentrations are sketched as dashed

lines in the pseudo-binary phase diagram Fe– TiB_2 calculated with ThermoCalc (TCFE7 database, adapted TiB_2 parameters) in Fig. 1a. The Ti contents were chosen in both cases about 17% over the stoichiometric amount required for TiB_2 in order to suppress the formation of Fe-borides and to neutralise any possible carbon (C) contamination by the formation of Ti-carbides [30]. Four synthesis techniques were employed in this work to achieve various solidification rates as sketched in Fig. 1b: (i) A differential scanning calorimetry (DSC) setup, heating and cooling 150 mg charges at a rate of 1 K min^{-1} . (ii) Arc melting (ARC) of 20 g charges under Ar on a water-cooled plate using four times re-melting and flipping, resulting in button shaped samples of about 20 mm diameter and 8 mm thickness. The cooling rate of about 5 K s^{-1} was estimated from thermal imaging after switching off the arc. (iii) Vacuum induction melting (VIM) of 800 g charges in an Al_2O_3 crucible under Ar and casting in a water-cooled copper mould of $20 \times 20 \times 200 \text{ mm}^3$ internal dimension. The cooling rate was measured with thermocouples inserted in the mould to be about 10 K s^{-1} . (iv) Levitation melting of 5 g charges under Ar, coupled with a splat cooling device (SPLAT) using polished Cu-plates, resulting in about $60 \mu\text{m}$ thick foils and a cooling rate of about $5 \times 10^7 \text{ K s}^{-1}$ according to literature data [36]. The solidification routes are named throughout this work according to the abbreviations given above. VIM and ARC experiments were carried out using high purity ($>99.99 \text{ wt.}\%$) raw materials, SPLAT and DSC experiments were performed with material cut from ARC samples. Wet chemical analysis of the VIM melts yielded oxygen and C concentrations for the hypo-eutectic alloy of 0.01 and 0.08 wt.%, respectively, and 0.03 and 0.13 wt.% for the hyper-eutectic material. In all melting experiments the materials were heated to at least $1600 \text{ }^\circ\text{C}$ to ensure complete liquefaction and dissolution of TiB_2 particles.

Microstructure characterisation was carried out by optical microscopy (OM, Zeiss Axiophot), scanning electron microscopy (SEM; Jeol JSM-6500F), X-ray diffraction (XRD; Seifert ID002), transmission electron microscopy (TEM; Jeol-2200FS) and atom probe tomography (APT; Imago LEAP 3000X HR, in voltage mode at 200 kHz pulse frequency with a pulse fraction of 15% and a detection rate of 0.5% as evaporation parameters, sample base temperature of 60 K). The SEM was equipped with a field emission gun, EDAX energy dispersive X-ray spectroscopy (EDX) system and a TSL electron backscatter diffraction (EBSD) system. Site specific sample preparation for TEM and APT was performed with a focussed ion beam system (FIB; FEI Helios Nanolab 600i); to

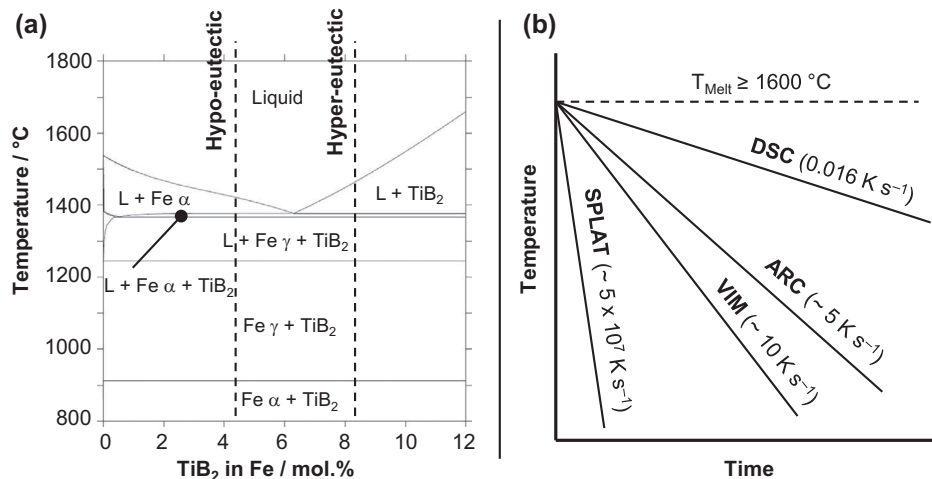


Fig. 1. (a) Section of the pseudo-binary Fe– TiB_2 phase diagram calculated with ThermoCalc, the two alloy compositions of this study are sketched as dashed lines. (b) Schematic cooling curves of the different solidification experiments. DSC: differential scanning calorimetry; ARC: arc melting; VIM: vacuum induction melting; SPLAT: levitation melting coupled with splat cooling.

minimise Gallium implantation a final milling of the tip was performed with low ion energies of 5 kV. The fraction and shape of particles were determined using image analysis (ImageJ software) on SEM and TEM micrographs.

Mechanical properties were probed by automated microhardness measurements, using a Fischerscope with a Vickers-type indenter and a load of 200 mN. A minimum of 100 indentations were placed per sample with a spacing of 50 μm between the indents.

4. Results

4.1. Microstructure

SEM micrographs in backscatter electron contrast obtained for the different cooling rates for the hypo-eutectic Fe–TiB₂ alloy are compiled in Fig. 2, providing overview pictures on the left and higher magnification pictures on the right hand side. After very slow cooling (DSC, Fig. 2a) a eutectic matrix (TiB₂; dark/Fe α ;

bright) containing a homogeneous distribution of ellipsoidal particle free areas about 100–500 μm in size can be observed. The eutectic TiB₂ particles are of irregular morphology with fine and sharp edged lamellas of about 1 μm in width and an average aspect ratio of about 2.2, resulting in a volume fraction for the eutectic areas of about 12.5 vol.% of particles (9.6 vol.% for the entire sample). Only in few areas coarser hexagonal shaped particles can be observed. Increasing the cooling rate (ARC sample, Fig. 2b) led to a disturbance of this quasi-ideal hypo-eutectic microstructure, rendering the eutectic lamellas more irregular in shape, size and relative alignment, and increasing the number of coarse particles. The fraction of particles is with 9.7 vol.% almost identical as that obtained for the DSC sample. A further increased cooling rate provided by VIM melting and casting (Fig. 2c) rendered the microstructure into a dispersion of irregular shaped particles, ranging in length from less than 1 μm to more than 10 μm and an aspect ratio between 1.4 and 1.9. No noticeable difference between top and bottom of the 200 mm long VIM cast specimen can be observed, with particle fractions of 10.4 and 10.9 vol.%,

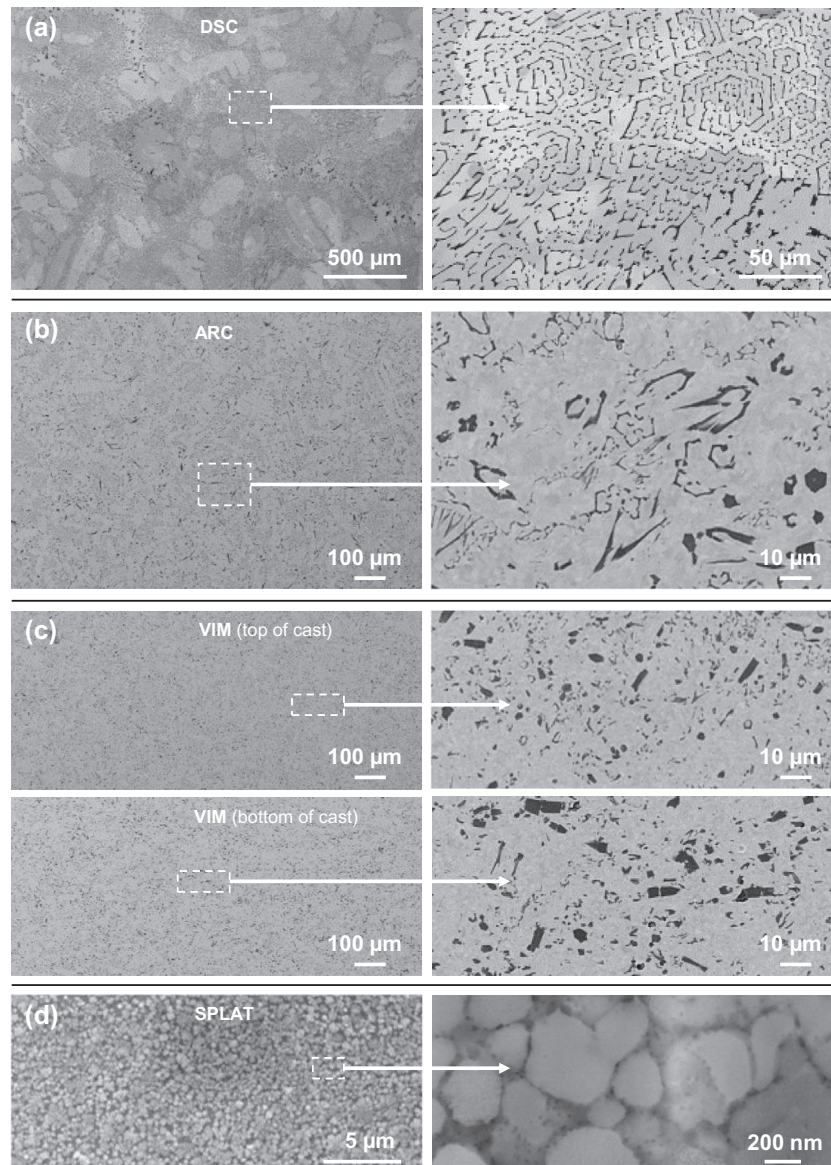


Fig. 2. SEM images of the microstructures obtained for different solidification rates of the hypo-eutectic alloy.

respectively. The highest cooling rate of the SPLAT samples (Fig. 2d) led to a sub-micron grained matrix with a complex intergranular nanostructure.

Concerted increase of Ti and B amounts to a hyper-eutectic composition led to microstructures as presented in Fig. 3. The eutectic fractions of the TiB_2 particles are roughly similar in morphology and size compared to those formed in respective experiments using a hypo-eutectic composition (Fig. 2). The additionally formed primary particles, however, are precipitated continuously from the melt over a wider temperature range compared to the eutectic fractions (Fig. 1a). Consequently their low density makes their dispersion strongly dependent on the applied cooling rate: The slow solidification of the DSC experiments (Fig. 3a) yields a layer of coarse primary particles (with an average diameter of about $60\ \mu\text{m}$ and an aspect ratio of 1.5) having floated to the top of the specimen. It should be noted that the eutectic particles underneath this 'crust' have a similar aspect ratio, but less sharp cornered lamellae and lacking the angled or branched morphology compared to those observed in the

respective hypo-eutectic DSC experiments (Fig. 2a). The respective eutectic particle fraction, however, is with a fraction of 11.2 vol.% comparable, the entire sample (primary and eutectic particles) contains 18.3 vol.%. The increased cooling rate of the ARC experiments (Fig. 3b) leaves the total particle fraction virtually unchanged (17.6 vol.%) but renders the microstructure more homogenous. Nevertheless a pronounced agglomeration of the coarse primary particles – which are now about one order of magnitude smaller than observed for the respective DSC experiments – can be detected. This holds true as well for the slightly faster cooled VIM samples (Fig. 3c), but now also a strong difference between top and bottom of the solidified ingot can be observed: while the top of the cast exhibits a microstructure close to the hyper-eutectic ARC samples (Fig. 3b), the bottom microstructure is almost identical to that of the hypo-eutectic VIM specimens (Fig. 2c), indicating that most of the primary particles have floated to the top of the cast at this cooling rate. This is expressed in the total particle fractions, which yield 17.1 vol.% for the bottom and 29.7 vol.% for the top of the cast. In the ultra-fast solidified SPLAT

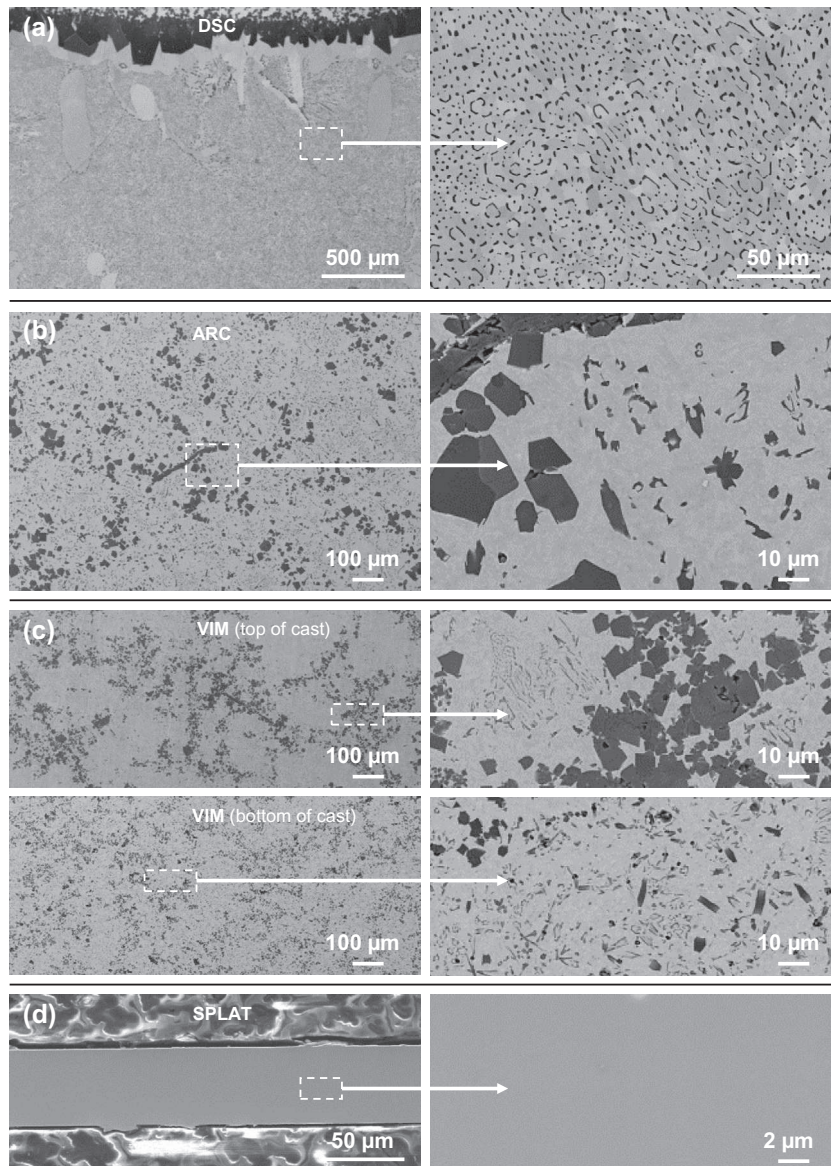


Fig. 3. SEM images of the microstructures obtained for different solidification rates of the hyper-eutectic alloy.

samples, the formation of particles has been apparently completely suppressed, as neither primary nor eutectic components could be observed (Fig. 3d).

Phase identification experiments for the intermediate (ARC, VIM) and slow cooling rate experiments (DSC) are exemplified on a hyper-eutectic ARC sample (Fig. 4); here, the colour coded EBSD phase map with image quality data superimposed in grey scale (Fig. 4a) confirms Fe α (red) and TiB₂ (green) as the main microstructure constituents. Only trace amounts (less than about 0.1 vol.%) of Titanium carbides (TiC) of around 1 μm in diameter were found. As shown on the corresponding EBSD inverse pole figure map (Fig. 4b), the TiB₂ grains are randomly oriented and the large primary particles are often polycrystalline. TEM investigations (Fig. 4c) confirmed the EBSD results and showed no evidence

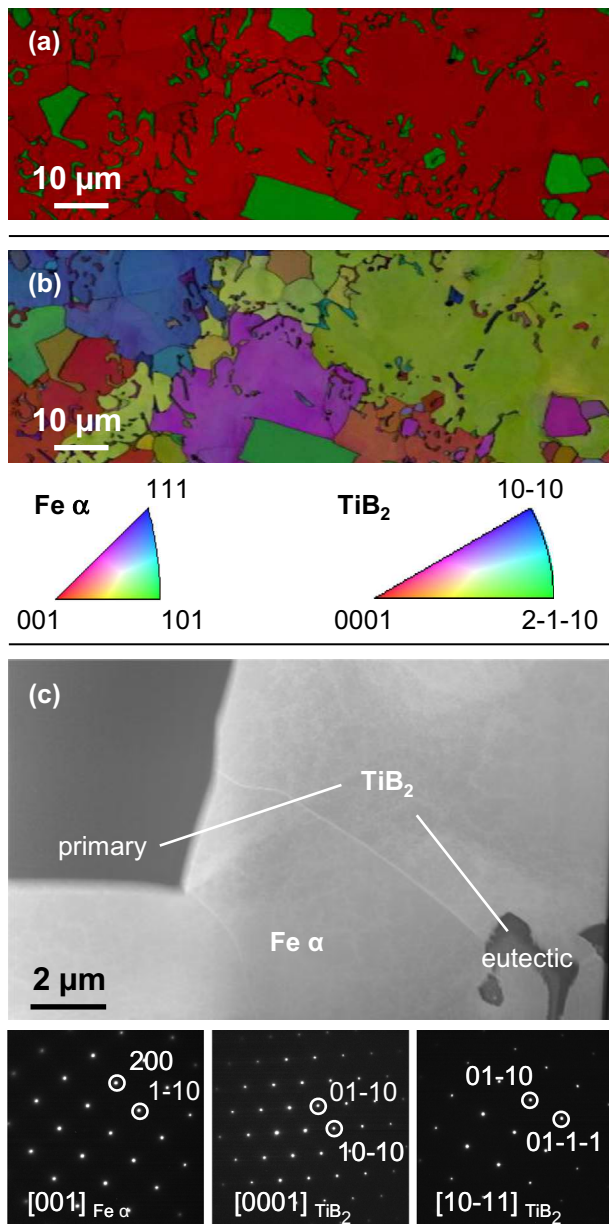


Fig. 4. Phase identification of the hyper-eutectic ARC sample: (a) EBSD phase with superimposed image quality map (Fe α red, TiB₂ green). (b) EBSD inverse pole figure with superimposed image quality map and corresponding orientation triangles. (c) STEM HAADF image and corresponding TEM SAD patterns. (For interpretation of the references to colour in this figure legend, the reader is referred to the web version of this article.)

of fine-scaled carbides, Fe borides or intermetallic phases within the Fe matrix or at the interface between Fe α and TiB₂.

The more complex microstructure of the rapidly solidified SPLAT samples shown in Figs. 2 and 3 was investigated in more detail using high resolution techniques (Fig. 5). TEM investigations (Fig. 5a) showed the hyper-eutectic alloy to consist of an ultra-fine grained ferritic matrix with a complex, most probably multiphase Ti-rich intergranular microstructure. BF-TEM analysis explained why the observed HAADF contrast is reversed (the HAADF contrast of the Ti-rich compound should appear darker than that of ferrite, as in the SEM BSE images of Fig. 2d). Acquired diffraction patterns reveal overlapping of individual diffracted spots (corresponding to Fe α $D_{110} = 0.203$ nm) with a strongly diffused ring of the amorphous Ti-rich phase (most probably TiB₂ $D_{110} = 0.201$ nm; insert in the diffraction pattern represents the rotational average of intensities). That amorphous component results in additional, stronger-scattering of electrons at a specific angle that also corresponds to the ferritic phase. Thus the overall contrast of the intergranular microstructure appears brighter than that of ferrite. Neither TEM diffraction analysis (insert in Fig. 5a) nor XRD analysis (Fig. 5b) fully revealed the phases present, yet the results are similar to those found in the interface region of steel/Ti explosion clads, which are formed under similar non-equilibrium conditions [37]. XRD and TEM analysis of the hyper-eutectic alloy (Fig. 5c) showed the material to be (quasi) amorphous as will be discussed in the following. Several APT measurements (see examples in Fig. 5d) revealed it to be chemically homogeneous. The concentration profiles taken along the region highlighted in the reconstruction overview of the different elements remain constant while there are no indications of chemical partitioning. A statistical analysis [38] over the entire reconstructed volume quantitatively supports the presence of a homogeneous state. Frequency distribution analysis elucidated that the experimental distribution closely follows a binomial form. The obtained confidence analyses based on the chi-square and *P*-values showed a perfect random mixing of the elements in the alloy. The average composition of the alloy determined by APT is close to the nominal composition (Table 1). The over-quantification of Ti and the consequent under-quantification of the B-concentration can be related to preferential field evaporation or retention of the related atoms or due to the presence of multiple events at the detector at a specific time. Additionally detected impurities of C (up to 0.1 at.%), silicon and aluminium (less than 0.05 at.%) most probably stem from the casting or the sample preparation process.

The amorphous, particle-free hyper-eutectic SPLAT alloy (Fig. 5c and d) was additionally annealed at 1000 °C (no holding time) with a heating and cooling rate of 20 K min⁻¹ under Ar (Fig. 6). XRD measurements indicated that this heat treatment resulted in a constitution similar to that of the VIM casts, i.e. crystallisation of Fe α and TiB₂. TEM investigations (Fig. 6b) confirmed this microstructure build-up, and revealed that TiB₂ precipitated as nano-sized particles (20–100 nm diameter) of about equilibrium fraction (about 19 vol.%) in a ferritic matrix with an average grain size of about 200 nm. Corresponding APT results from such an additionally annealed hyper-eutectic SPLAT sample are summarised in Fig. 7. As shown in Table 1 the ferritic matrix contains impurities of Ti, B and C in amounts less than 0.1 at.% each (overview in Fig. 7a). Moreover, the matrix composition is uniform through all the analysed regions and samples. Higher amounts (up to 1.5 at.%) of Ti and B were found at a matrix grain boundary (Fig. 7b). The two Ti and B-rich regions (Fig. 7c and d) exemplify the characteristics of the TiB₂ particles. Although the particles are mostly spherical, characteristic facets of the prismatic morphology can be observed in several of the reconstructed volumes. Their composition (Table 1) yields an under-stoichiometric atomic B/Ti ratio of about 1.55. This increased amount of Ti could be expected

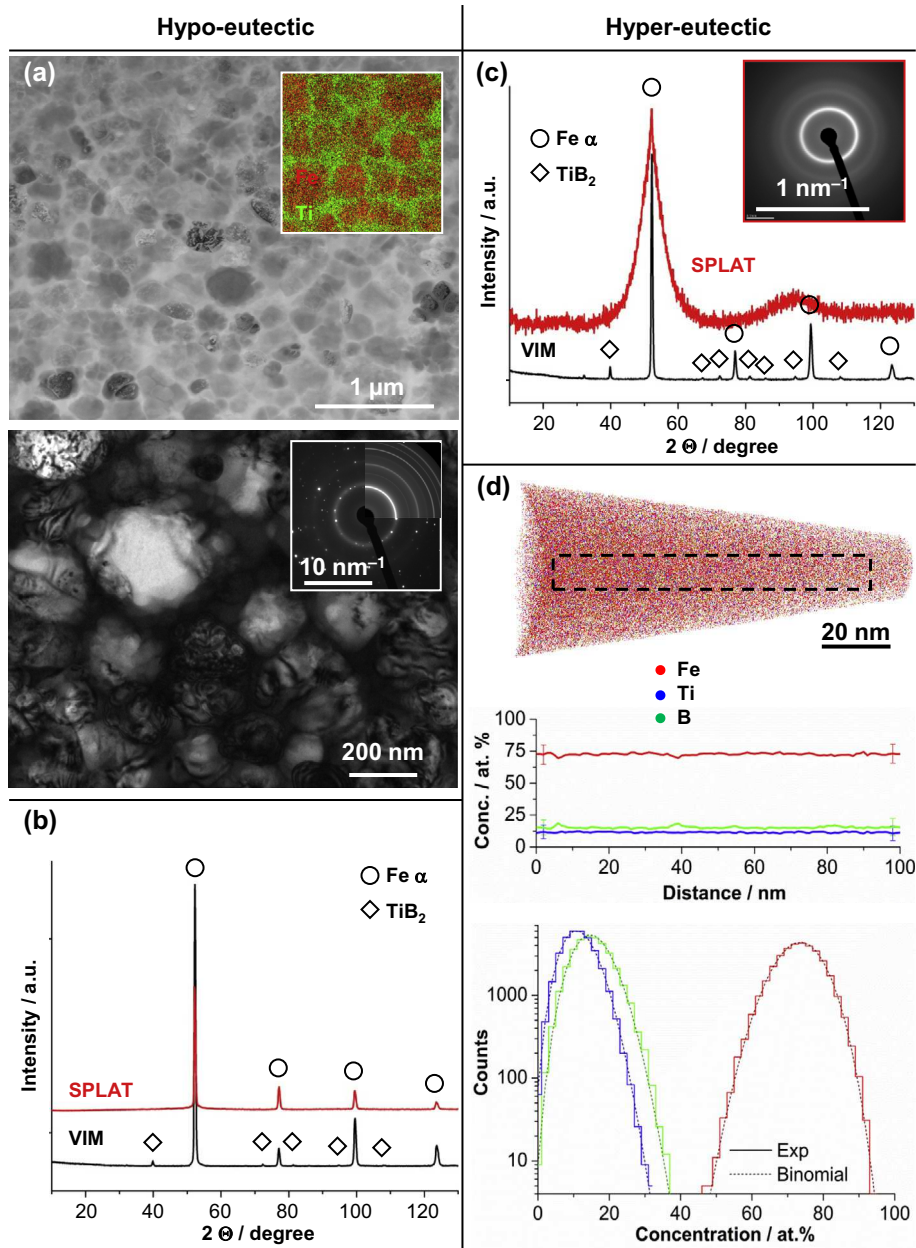


Fig. 5. Detailed analyses of the SPLAT samples (a, b hypo-eutectic; b, c hyper-eutectic material): (a) STEM HAADF micrograph (top) and BF-TEM analysis (bottom) showing ultra fine ferritic grains separated by Ti-rich phase (EDX map insert) with a diffuse ring on the diffraction pattern (SAD insert). (b) XRD pattern together with VIM data, only Fe α could be indexed for the SPLAT sample. (c) TEM and XRD analysis revealing amorphisation of the material. (d) APT analysis showing homogeneous distribution of Fe, Ti and B (from top to bottom: APT reconstruction, concentration profile along the selected region in dashed lines and frequency distribution analysis). SPLAT: levitation melting coupled with splat cooling.

Table 1

Chemical compositions (at.%) of the hyper-eutectic material after ARC and SPLAT experiments as well as matrix and particle compositions of a SPLAT sample annealed at 1000 °C. SPLAT: levitation melting coupled with splat cooling.

Element	ARC (wet chemical)	SPLAT as-cast (APT)	SPLAT annealed (APT)	
			Matrix	Particle
Fe	Balance	72.9	99.81	1.8
Ti	10.01	11.7	0.11	38.4
B	16.93	15.4	0.08	59.7

as a B/Ti atomic fraction of 1.69 was introduced in the master alloy, there were no traces of this element in the matrix and a compositional range of Ti and B has been reported for TiB₂ [30]. The

composition inside the particles appears to be inhomogeneous as concentration variations are visible (Fig. 7c) and Ti and B show larger error bars. Fe in concentrations up to 2 at.% was found inside the TiB₂ particles, though also not distributed homogeneously (Fig. 7d). The higher Fe concentration is found approaching the centre of the TiB₂ particles from where ordered needle-shaped structures spread towards the limits of the particle (Fig. 7a). Most of the quantified C is segregating to form presumably Ti-carbides, either as ~5 nm platelets in the matrix (white arrow in Fig. 7a) or covering a facet of the particle at its interface with the matrix (Fig. 7d). The latter corroborates the formation of TiC covering the basal plane of TiB₂ particles as reported by Cha et al. [39] in composites with much larger features and higher amount of C.

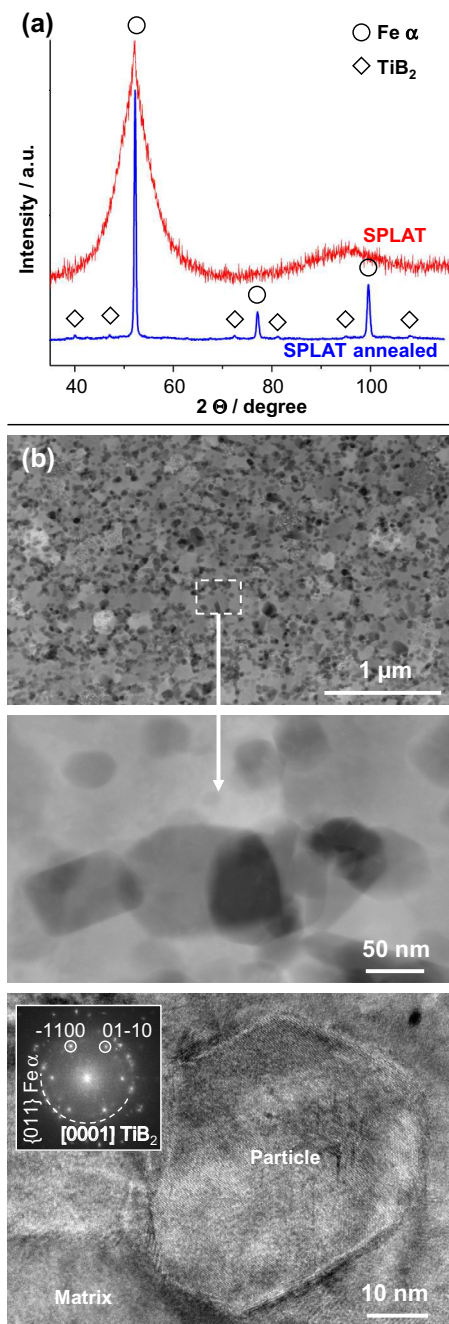


Fig. 6. Microstructural analysis of a hyper-eutectoid SPLAT sample annealed at 1000 °C: (a) XRD analysis showing the effect of annealing on the structure of the material, i.e. crystallisation of TiB_2 particles in a $\text{Fe } \alpha$ matrix. (b) HAADF STEM micrographs at different magnification (top, middle) and HR-TEM analysis (bottom) with corresponding fast-fourier-transform (insert), corroborating the XRD results. SPLAT: levitation melting coupled with splat cooling.

4.2. Mechanical properties

Microhardness testing results are plotted as a function of the solidification rate in Fig. 8. The average values for the hypo-eutectic material (Fig. 8a) increase with the cooling rate from about 190 HV0.02 for the DSC sample to about 480 HV0.02 for the SPLAT sample while the scatter remains constant with about ± 50 HV0.02.

In case of the hyper-eutectic material (Fig. 8b) the average microhardness of the DSC, ARC and VIM samples remains roughly constant at about 400 HV0.02, with only the amorphous SPLAT

sample showing a slight increase of about 200 HV0.02. The much larger scatter for the hyper-eutectic alloys reflects the pronounced inhomogeneity of the microstructures (Fig. 3): the increasing coarsening and agglomeration of the primary TiB_2 particles with decreasing cooling rates make them more likely to be probed without influences of the much softer ferritic matrix. When only the eutectic zone is probed in the DSC sample, i.e. below the top layer of up-floated primary particles, very low values with little scatters (170 ± 40 HV0.02) were found, matching the homogeneously dispersed eutectic microstructure (Fig. 3a). Annealing of the amorphous SPLAT sample decreased the average microhardness – despite the very small grain sizes (Fig. 6) – back to levels of the DSC, ARC and VIM experiments.

5. Discussion

In-situ liquid metallurgy Fe– TiB_2 MMCs could be successfully produced over a wide range of controlled solidification rates (Fig. 1). The particle fractions for the slowest cooling rates (DSC experiments; 1 K min^{-1}) of 9.6 vol.% and 18.3 vol.% for the hypo- and hyper-eutectic alloys, respectively, are in reasonable agreement with literature data [28] and Calphad predictions (10 and 20 vol.%, respectively). The observed morphologies, i.e. lamellar eutectic and sharp-edged, coarser primary TiB_2 particles (Fig. 2a and 3a), are expected for such solidification conditions close to thermodynamic equilibrium [40,41]. Fraction, size and most importantly, also the morphology of the TiB_2 particles can be efficiently engineered by using different solidification rates:

Higher solidification rates from VIM and ARC experiments (Figs. 2b, c and 3b, c) leave the particle fractions almost unaffected, but result in deteriorating of the fine lamellar eutectic structure of the DSC experiments towards coarser and sharp edged particles. The already large primary particles from the hyper-eutectic alloy are refined by the increased solidification rates, but they still tend to float (as they do in DSC experiments, Fig. 3a) and agglomerate during solidification due to their lower density. The observed microstructures are thus in fact close to those reported in previous works which used industrially established liquid metallurgy synthesis processes such as block or strip-casting [25,32,39]. The corresponding mechanical properties of such HMS, however, are not yet satisfactory for structural applications. The tensile elongation was for instance found to be almost halved by the incorporation of just 10 vol.% TiB_2 with a morphology and dispersion comparable to our VIM and ARC experiments [25]. While the exact interaction between soft and ductile metallic matrix and the hard and stiff ceramic particles during co-deformation is complex and still not fully understood [31,32,42,43], the unfavourable ductility can be assumed to be mainly caused by the irregular dispersion of comparatively large and sharp-edged particles acting as stress concentrators. This is corroborated by results from powder metallurgy experiments, where the dispersion of particles is easily controlled, but their morphology and size and thus the bulk materials ductility are nevertheless not satisfactory [44]. Despite the use of fine-grained particle-powders and mechanical atomisation (ball milling), the formation of sharp-edged particles larger than about $3 \mu\text{m}$ could not be avoided, as they apparently agglomerated during mechanical mixing and/or coarsened during subsequent sintering of the powders at elevated temperatures [44].

Powder metallurgy fabrication methods as well as liquid metallurgy synthesis with such ‘intermediate’ solidification rates thus seem not to be ideally suited for producing Fe– TiB_2 based MMCs with an optimised property profile. This holds especially true for hyper-eutectic alloys which are desirable for achieving high E/ρ ratios due to their high particle fractions. We find, however, that precisely for these most attractive compositions, two different

solidification routes enable the creation of extremely promising microstructures:

- (1) By strongly accelerating the solidification as in our SPLAT experiments, the formation of TiB_2 can be completely suppressed and a metallic glass is formed (Figs. 3d and 5c) due to the large B and Ti concentrations with their differing atomic radii compared to Fe [45]. Annealing of this fully homogeneous amorphous material (Fig. 5d) at 1000 °C results in crystallisation of a fine grained ferritic matrix and the precipitation of nano-scaled TiB_2 particles within (Figs. 6 and 7). This allows obtaining compound materials with an optimum dispersion of particles in small sizes that are not even accessible by powder metallurgy and with particle contents roughly matching the equilibrium fraction required for achieving the desired effects on stiffness and density. This is of interest in view of ODS steels, which owe their favourable property profile from similarly sized and dispersed particles [4,46,47]. Whether the observed microstructures as well as the corresponding soft and homogeneous microhardness profile (Fig. 8b) of this nano-structured HMS translate into improved mechanical

properties (e. g. regarding ductility and toughness) is the subject of future investigations. While no systematic investigations were conducted in this work, the annealed hyper-eutectic SPLAT foils could be bent sharply to angles larger than about 30° without fracture. Although more work is needed to investigate the necessary cooling rate for the suppression of particle formation as well as for identifying optimal kinetics and constitutional pathways of the TiB_2 formation during subsequent annealing (e.g. glass transition and crystallisation temperatures), a wide range of easily controllable microstructure build-ups should be possible as the particle precipitation and matrix-crystallisation seem to take place at industrially compliant time scales (minutes to hours) and strive towards thermodynamic equilibrium (and not a metastable state). Industrial processing could be achieved by rapid solidification techniques such as thin-slab casting or, most promisingly, novel additive manufacturing routes [48,49].

- (2) Another pathway for optimised Fe– TiB_2 HMS is found on the other side of the spectrum of the cooling rates studied here: Extremely slow solidification without any – inductive or mechanical – stirring, as for instance obtained in a

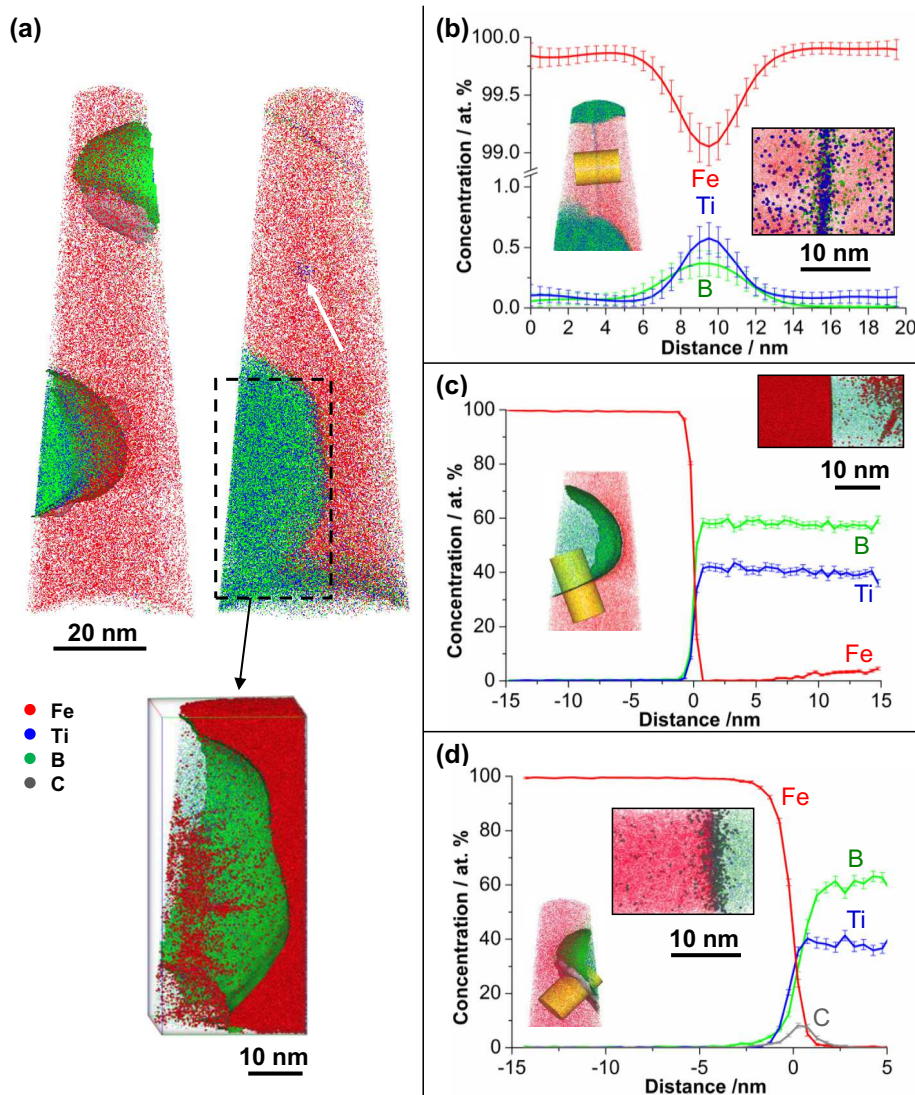


Fig. 7. APT analysis of a hyper-eutectoid SPLAT sample annealed at 1000 °C: (a) overview of reconstructed samples. (b–d) Chemical concentration profiles across specific interface regions: (b) matrix grain boundary, (c, d) matrix-particle interfaces. SPLAT: levitation melting coupled with splat cooling.

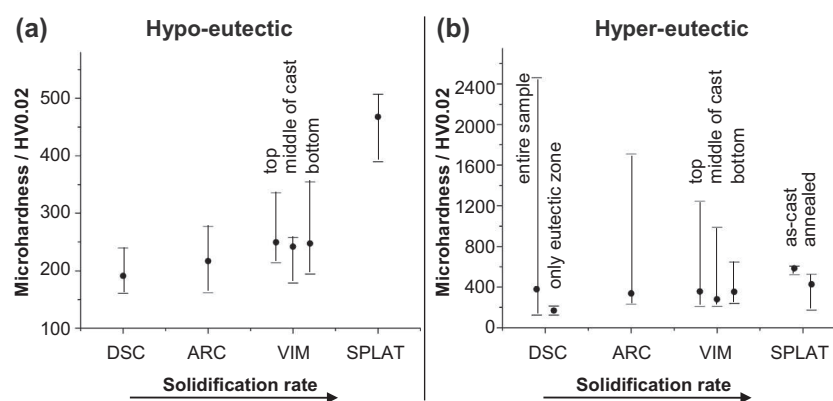


Fig. 8. Microhardness data for the hypo-eutectic (a) and hyper-eutectic (b) materials for different solidification rates. DSC: differential scanning calorimetry; ARC: arc melting; VIM: vacuum induction melting; SPLAT: levitation melting coupled with splat cooling.

Tammann-furnace or a large block-cast in sand-moulds, allows all the coarse primary TiB_2 particles to float to the top of the cast (as observed in our DSC experiments; Fig. 3a). When this ‘crust’ is subsequently removed along with the head of the cast and its shrinkage, a fully eutectic bulk material is obtained with micron-sized eutectic TiB_2 particles in optimum dispersion, for which our microhardness measurements yield excellent homogeneity (i.e. lowest scatter) at low hardness levels. Interestingly, the eutectic particles are also of more compliant, spherical shape than those synthesised in the hypo-eutectic alloy solidified under similar conditions (Fig. 2a). After the solidification is complete, the cooling rate may be adapted to achieve desired matrix microstructures. Additional alloying elements could be utilised in future HMS developments to shift the eutectic point (and thus the amount of usable particles) to higher TiB_2 concentrations as well as to further modify the eutectic morphology as demonstrated for Al–Si alloys [50–52]. Targeting eutectic concentrations directly is possible but renders the production susceptible to concentration-induced instabilities, i.e. could lead to the formation of undesired hypo- or hyper-eutectic microstructure fractions. As a variation of this processing route, the crust of extremely hard primary TiB_2 particles could also be exploited rather than removed serving as a self-assembling, wear-resistant surface layer on the cast-parts such as for drill discs and other mineral handling applications [9], with the option to tailor the surface layer and its (possibly gradual) transition towards the bulk. Coatings of other (steel) substrates with a hyper-eutectic Fe– TiB_2 -based alloy via spraying or welding processes also seem promising as the boride particles – unlike carbides – should not interact intensively with other desired matrix alloying elements such as Cr.

6. Summary and conclusions

We systematically studied the effect of the solidification rate on the microstructure and mechanical properties of Fe– TiB_2 composites formed in-situ from Fe–Ti–B melts in hypo- and hyper-eutectic concentrations. Within the wide investigated range of cooling rates, spanning from less than 1 to more than 10^7 K s^{-1} , strongly differing microstructures were obtained, opening novel pathways for the cost-effective production of stiff and ductile MMCs for lightweight structural applications. The following conclusions can be drawn:

- (1) Slow cooling rates close to thermodynamic equilibrium (about 0.016 K s^{-1}) result in particle fractions as predicted by Calphad-methods. Increasing the solidification rate to values closer to industrial steel production conditions (about $5\text{--}10 \text{ K s}^{-1}$) deteriorates the morphology of the eutectic lamellae and refines the primary particles. Very high cooling rates (about $5 \times 10^7 \text{ K s}^{-1}$) lead to fine-scaled metastable microstructures in case of hypo-eutectic alloys and amorphisation of hyper-eutectic materials.
- (2) Hyper-eutectic alloys are most interesting due to their high stiffness/density ratio. Intermediate cooling rates, however, result in unfavourable microstructures, especially as the density-induced floatation and agglomeration of the still coarse and sharp-edged primary particles are difficult to control. However, two types of processing strategies enable the formation of promising microstructure build-ups.
- (3) Very slow cooling allows the floatation of the primary particles to the top of the cast. The resultant layer of coarse and hard TiB_2 particles can then either be easily removed for retaining large, fully eutectic bulk material containing micron-sized eutectic TiB_2 particles in optimum dispersion, or be kept and utilised as a wear resistant surface.
- (4) Annealing of very fast solidified, amorphous materials leads to evenly dispersed and nano-scaled precipitation of TiB_2 particles in an ultra-fine grained ferritic matrix.
- (5) Future work is concerned with studying the influence of alloying elements on the critical cooling rate for particle suppression as well their effect on particle morphology. Furthermore, the kinetic pathway for crystallisation and the precipitation sequence from the amorphous state will be studied in more detail, as well as the resultant mechanical properties.

Acknowledgements

Dr. H. Zhang is gratefully acknowledged for support with mechanical testing, microstructure characterisation and valuable discussions. M. Kulse and B. Breitbach are acknowledged for their support with synthesis and XRD analysis, as is Thermocalc Sweden for support regarding the thermodynamic calculations.

References

- [1] R. Hasenhündl, S. Eglsäer, H. Orthaber, R. Tanzer, W. Schützenhöfer, R. Schneider, *BHM* 154 (2009) 5.
- [2] M.J. Duarte, J. Klemm, S.O. Klemm, K.J.J. Mayrhofer, M. Stratmann, S. Borodin, A.H. Romero, M. Madinehei, D. Crespo, J. Serrano, S. Gerstl, P. Choi, D. Raabe, *F.U. Renner, Science* 341 (2013) 6144.

- [3] K.H. Lo, C.H. Shek, J.K.L. Lai, *Mater. Sci. Eng.*, R 65 (2009) 39.
- [4] K.D. Zilnyk, H.R.Z. Sandim, R.E. Bolmaro, R. Lindau, A. Möslang, A. Kostka, D. Raabe, *J. Nucl. Mater.* 448 (2014) 1.
- [5] S. Ukai, S. Mizut, M. Fujiwara, T. Okuda, T. Kobayashi, *J. Nucl. Sci. Technol.* 39 (2002) 7.
- [6] D. Raabe, D. Ponge, O. Dmitrieva, B. Sander, *Adv. Eng. Mater.* 11 (2009) 547.
- [7] N. Nakada, T. Tsuchiyama, S. Takaki, D. Ponge, D. Raabe, *ISIJ Int.* 53 (2013) 12.
- [8] S. Zaeferrer, J. Ohlert, W. Bleck, *Acta Mater.* 52 (2004) 2765.
- [9] H. Berns, W. Theisen, *Eisenwerkstoffe Stahl und Gusseisen*, Springer Verlag, Berlin, Heidelberg, 2006.
- [10] H.K.D.H. Bhadeshia, R. Honeycombe, *Steels Microstructure and Properties*, third ed., Butterworth-Heinemann, Oxford UK, 2006.
- [11] M.F. Ashby, *Materials Selection in Mechanical Design*, Butterworth-Heinemann, Burlington, MA, USA, 2005.
- [12] S. Münstermann, W. Bleck, *Mater. Meas.* 47 (2005) 337.
- [13] G.R. Speich, A.J. Schwoeble, W.C. Leslie, *Metall. Trans.* 3 (1972) 2031.
- [14] H. Springer, D. Raabe, *Acta Mater.* 59 (2011) 1586.
- [15] G. Frommeyer, U. Brück, *Steel Res. Int.* 77 (2006) 627.
- [16] Bausch M. et al. RFCS project report CT-2006-00027 (MnAl steel) June 2009.
- [17] J.E. Allison, G.S. Cole, *JOM* 01 (1993) 19.
- [18] J.W. Kaczmar, K. Pietrzak, W. Wosinaski, *J. Mater. Proc. Technol.* 106 (2000) 58.
- [19] D.B. Miracle, *Compos. Sci. Technol.* 65 (2005) 2526.
- [20] S.C. Tjong, Z.Y. Ma, *Mater. Sci. Eng.*, R 29 (2009) 49.
- [21] G.B. Veeresh Kumar, C.S.P. Rao, N. Selvaraj, *J. Min. Mater. Charact. Eng.* 10 (2011) 59.
- [22] B. Maruyama, W.H. Hunt, *JOM* 11 (1999) 59.
- [23] H. Nakanishi, K. Kakiyama, A. Nakayama, T. Murayama, *JSAE Rev.* 23 (2002) 365.
- [24] P.K. Rohatgi, R. Asthana, S. Das, *Int. Met. Rev.* 31 (1986) 115.
- [25] Feng Y. PhD thesis, RWTH Aachen, 2013.
- [26] G. Arth, A. Samoilov, *BHM* 157 (2012) 306.
- [27] R.G. Munro, *J. Res. Natl. Inst. Stand. Technol.* 105 (2000) 709.
- [28] A.K. Shurin, V.E. Panarin, *Izv. Akad. Nauk SSSR Met.* 5 (1974) 235.
- [29] Arcelor Research group; Patent EP 1 897 963 A1, *Bulletin* 2008, 20.
- [30] K. Tanaka, T. Saito, *J. Phase Equilib.* 20 (1999) 207.
- [31] Z. Kulinowski, T.M.T. Godfrey, A. Wisbey, P.S. Goodwin, F. Langlais, H.M. Flower, J.G. Zheng, D.P. Davies, *Mater. Sci. Technol.* 16 (2000) 1453.
- [32] Z. Hadjem-Hamouche, J.P. Chevalier, Y. Cui, F. Bonnet, *Steel Res. Int.* 83 (2012) 538.
- [33] R. Rana, *Can. Metall. Q.* 53 (2014) 241.
- [34] R. Rana, C. Liu, *Can. Metall. Q.* 53 (2014) 300.
- [35] P. Muro, S. Gimenez, I. Iturriza, *Scripta Mater.* 46 (2002) 369.
- [36] R.C. Ruhl, *Mater. Sci. Eng.*, A 1 (1967) 313.
- [37] J. Song, A. Kostka, M. Veehmayer, D. Raabe, *Mater. Sci. Eng.*, A 528 (2001) 2641.
- [38] M.J. Duarte, A. Kostka, J.A. Jimenez, P. Choi, J. Klemm, D. Crespo, D. Raabe, F.U. Renner, *Acta Mater.* 71 (2014) 20.
- [39] L. Cha, S. Lartigue-Korinek, M. Walls, L. Mazerolles, *Acta Mater.* 60 (2012) 6382.
- [40] G. Gottstein, *Physical Foundations of Materials Science*, Springer Verlag, Berlin, 2004.
- [41] M. Asta, C. Beckermann, A. Karma, W. Kurz, R. Napolitano, M. Plapp, G. Purdy, M. Rappaz, R. Trivedi, *Acta Mater.* 57 (2009) 941.
- [42] N. Yang, I. Sinclair, *Metall. Mater. Trans. A* 34 (2003) 2017.
- [43] Bayraktar, E., Ayari, F., Katundi, D., Chevalier J.P., Bonnet F. Proceedings of the SEM Annual Conference, 2010 Indianapolis, Indiana USA.
- [44] Z. Kulinowski, A. Wisbey, T.M.T. Godfrey, P.S. Goodwin, H.M. Flower, *Mater. Sci. Technol.* 16 (2000) 925.
- [45] A. Inoue, *Acta Mater.* 48 (2000) 279.
- [46] C.A. Williams, E.A. Marquis, A. Cerezo, G.D.W. Smith, *J. Nucl. Mater.* 400 (2010) 37.
- [47] S. Pasebani, I. Charit, Y.Q. Wub, D.P. Butt, J.I. Cole, *Acta Mater.* 61 (2013) 5605.
- [48] E. Brandl, B. Baufeld, C. Leyens, R. Gault, *Phys. Proc.* 5 (2010) 595.
- [49] A. Gebhardt, *Generative Fertigungsverfahren, Rapid Prototyping-Rapid Tooling-Rapid Manufacturing*, Carl Hanser Verlag, München, 2007.
- [50] R. Aparicio, G. Barrera, G. Trapaga, M. Ramirez-Argaez, C. Gonzalez-Rivera, *Met. Mater. Int.* 19 (2013) 707.
- [51] A.K. Dahle, K. Nogita, S.D. McDonald, C. Dinnis, L. Luc, *Mater. Sci. Eng.*, A 413 (2005) 243.
- [52] Nave, M.D., Dahle, A.K., St. John, D.H. Magnesium technology; 2000.